Available online at www.sciencedirect.com
ScienceDirect
Trans. Nonferrous Met. Soc. China 35(2025) 2536−2552
Transactions of Nonferrous Metals Society of China
www.tnmsc.cn

Effect of different preheating treatments on dynamic recrystallization behavior of hot-compressed Mg−Gd−Y−Zn−Zr alloy

Liang LIU, Zhi-min ZHANG, Yong XUE

School of Materials Science and Engineering, North University of China, Taiyuan 030051, China

Received 22 May 2024; accepted 5 March 2025

Abstract: A Mg−13Gd−4Y−2Zn−0.5Zr (wt.%) alloy was selected as the experimental material. After preheating, initial microstructures with different long-period stacking ordered (LPSO) phase and β' phase distributions were obtained, and hot compression experiments were conducted. The effects of secondary phases on microstructure and dynamic recrystallization (DRX) behavior were investigated. The results revealed that the average grain size decreased from 70.93 to 31.53 μm, and the DRX volume fraction increased from 20.3% to 40.1% after the pre-annealing treatment. The average grain size of Sample S0 (pre-aging) decreased to 39.29 μm, and the DRX volume fraction increased by 79.8%, whereas the average grain size of Samples S1−S7 (pre-annealing + aging) slightly increased, and the DRX volume fraction slightly decreased. With increasing pre-annealing time, the width of the lamellar LPSO phase increased, which generated less dynamic precipitation during deformation and weakened the pinning effect. The DRX mechanism transformed from continuous dynamic recrystallization (CDRX, pre-homogenization sample) to particle-stimulated nucleation (PSN) + discontinuous dynamic recrystallization (DDRX, pre-annealing sample). After the pre-aging treatment, the reticular structure effectively pinned the dislocations and delayed the nucleation and growth of DRX grains. The DRX mechanism changed from the original CDRX+PSN (pre-aging sample) to DDRX (pre-annealing + aging sample).

Key words: Mg−Gd−Y−Zn−Zr alloy; dynamic recrystallization; hot compression; β' phase; LPSO phase

1 Introduction

Mg alloys are favored by scholars because of their low density and high specific strength-to-stiffness ratio. However, owing to their hexagonal close-packed (HCP) structure, few slip systems are available at room temperature, which is not beneficial for plastic deformation [1−5]. Some scholars have improved the plasticity by adding rare earth (RE) elements. On the one hand, the addition of RE elements can effectively reduce the critical resolved shear stress (CRSS) for non-basal slip; on the other hand, the addition of RE elements and transition elements (such as Zn) can form a new type of long-period stacking ordered (LPSO) phase and improve the strength of the alloys [6−8].

The LPSO phase can be divided into two types according to its morphology: bulk and lamellar. The lamellar phase is generally located inside the grain; during the deformation process, the basal slip is hindered by kinking and bending to coordinate the deformation, which effectively improves the plasticity of the alloy [9−11]. The bulk LPSO phase can be crushed during deformation, which refines the grains and weakens the texture through the particle-stimulated nucleation (PSN) mechanism [8]. The continuous large lamellar LPSO in the hot-rolled Mg−9.7Gd−2.5Y−1.5Zn−0.4Zr (wt.%) alloy crystal strongly pins the dislocation motion. The migration of recrystallized grain boundaries along the basal plane and *c*-axis of lamellar LPSO

Corresponding author: Yong XUE, Tel: +86-19834400337, E-mail: yongxue395@163.com
https://doi.org/10.1016/S1003-6326(25)66831-2

is hindered. This makes it difficult to achieve a wide range of lattice rotations, which is not conducive to recrystallization and nucleation [12]. With respect to the relationship between the LPSO phase and twinning behavior, most researchers believe that the LPSO phase inhibits twinning [13]. However, some scholars hold the opposite view. ZHENG et al [6] reported that the combination of LPSO phase kink-induced lattice rotation and efficient Schmid factor under shear loading could stimulate twinning under strong shear deformation (a maximal shear strain of 3) in Mg−11Gd−4Y−2Zn−0.5Zr (wt.%) alloys.

For Mg−Gd−Y−Zn−Zr alloys, the β' phase is vital and is primarily introduced by aging heat treatment before deformation. During the deformation process, the β' phase gradually transforms into the β phase, which promotes dynamic recrystallization (DRX) through the PSN mechanism. The precipitation sequence of Mg−9Gd−4Y−2Zn−0.5Zr (wt.%) during aging at 200 °C is β'' (DO19) → β' (BCO) → β (FCC), and the increase in hardness of the alloy is mainly due to the increase in the volume fraction of the precipitated phases and the transition of the β'' phase to the β' phase [14]. ZHENG et al [15] reported that extruded Mg−9.5Gd−4Y−2.2Zn−0.5Zr (wt.%) alloys after the pre-aging treatment had a more homogeneous microstructure with a greater fraction of DRX grains, a yield strength (YS) of 408 MPa, an ultimate tensile strength (UTS) of 476 MPa, and an elongation (EL) of 8.3%. KANG et al [16] investigated the effects of the pre-aging treatment on the microstructure, texture, and mechanical properties of the Mg−6Zn−1Gd−1Er (wt.%) alloy. The results showed that the precipitation of the second-phase particles promoted the PSN mechanism during extrusion, which increased the volume fraction of DRX.

After the aging treatment, the special internal space structure of the Mg−9.55Gd−2.27Y−1.28Zn−0.55Zr−0.11Nd (wt.%) alloy, which consists of prismatic β' precipitates, basal γ' precipitates, and lamellar LPSO phases, effectively hinders dislocation motion and achieves high strength [17]. However, most of the current studies on Mg−RE alloys focus on a single phase with few studies on two-phase interactions. The mechanism of the effect of these two phases on the microstructure and DRX behavior during deformation remains unclear. In this work, a Mg−13Gd−4Y−2Zn−0.5Zr (wt.%) alloy was used as the experimental material to study the effects of different preheating treatments on the microstructure and DRX behavior of the LPSO and β' phases produced during hot pressing.

2 Experimental

Cylinders with dimensions of *d*8 mm × 12 mm were machined from 800 mm-diameter cast rods via wire cutting. As shown in Table 1, the samples were first homogenized at 520 °C for 32 h, water-cooled at 70 °C, and recorded as IT0 sample. The IT0 sample was subsequently annealed at 460 °C for 1, 4, and 7 h and subsequently air-cooled. Finally, these samples were aged at 200 °C for 112 h and air-cooled.

Table 1 Histories of different samples

Designation	History	Designation	History
IT0	520 °C, 32 h	T0	(520 °C, 32 h), compression
IT1	(520 °C, 32 h) + (460 °C, 1 h)	T1	(520 °C, 32 h) + (460 °C, 1 h), compression
IT4	(520 °C, 32 h) + (460 °C, 4 h)	T4	(520 °C, 32 h) + (460 °C, 4 h), compression
IT7	(520 °C, 32 h) + (460 °C, 7 h)	T7	(520 °C, 32 h) + (460 °C, 7 h), compression
IS0	(520 °C, 32 h) + (200 °C, 112 h)	S0	(520 °C, 32 h) + (200 °C, 112 h), compression
IS1	(520 °C, 32 h) + (460 °C, 1 h), (200 °C, 112 h)	S1	(520 °C, 32 h) + (460 °C, 1 h) + (200 °C, 112 h), compression
IS4	(520 °C, 32 h) + (460 °C, 4 h) + (200 °C, 112 h)	S4	(520 °C, 32 h) + (460 °C, 4 h) + (200 °C, 112 h), compression
IS7	(520 °C, 32 h) + (460 °C, 7 h) + (200 °C, 112 h)	S7	(520 °C, 32 h) + (460 °C, 7 h) + (200 °C, 112 h), compression

The samples were subjected to thermal compression experiments using a Gleeble−3500 system. The deformation temperature was 450 °C, the strain rate was 0.01 s^{-1}, and the compression amount was 60% with a cumulative strain of 0.916. Figures 1(a_1, a_2) show the detailed steps of deformation. The ends of the samples were covered with graphite flakes to minimize friction during hot compression. All the samples were heated at a rate of 5 K/s and subsequently held at the experimental temperature for 180 s to ensure uniform heat distribution. After the compression experiments, the samples were cooled with water, and stress−strain data were obtained.

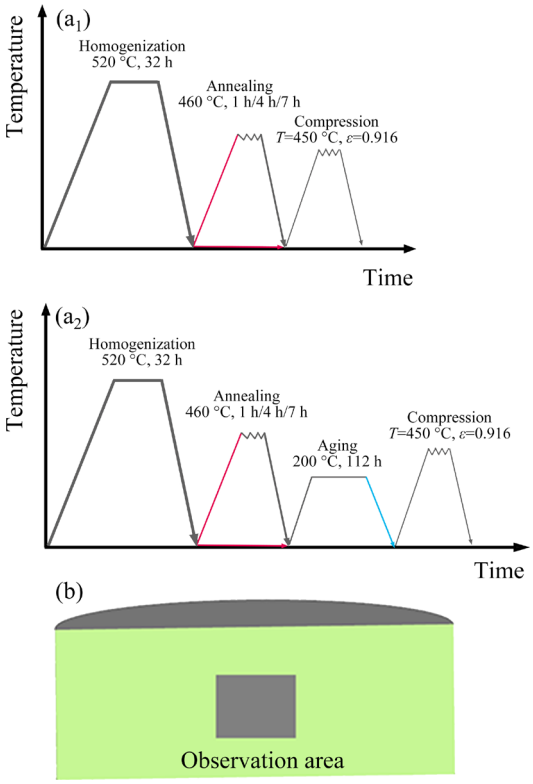

Fig. 1 Schematic illustration of experimental procedures (a_1, a_2), and specimen observation area (b)

Figure 1(b) shows the specific observation area, where the more drastically deformed region in the middle was selected as the observation location. The microstructures of the different samples were analyzed via optical microscopy (OM, Zeiss Axio Imager A2m) and scanning electron microscopy (SEM, Hitachi SU5000). First, the samples were mechanically polished using water-abrasive sandpaper of varying roughness values and etched with a solution of 1 g picric acid, 2 mL acetic acid, 14 mL alcohol, and 2 mL distilled water. Then, they were metallographically photographed using the optical microscope. Scanning electron microscopy (SEM) and electron backscatter diffraction (EBSD) were performed at an accelerating voltage of 20 kV, a working distance of 15 mm, and a tilt angle of 70°. The experimental results were post-processed using the Orientation Imaging Microscopy (OIM) Analysis 7.0 software from EDAX. The phase compositions of the alloys were analyzed via X-ray diffraction (XRD, Smart Lab) with Cu K_α radiation at 40 kV and 40 mA. The samples were prepared as single pieces with diameter of 43 mm and thickness of 30 mm and subjected to transmission electron microscopy (TEM, JEOL JEM-F200) at 200 kV.

3 Results

3.1 Initial microstructure

Figure 2 shows SEM images of different samples before deformation and the corresponding EDS analysis, which verified that the gray phase was the LPSO phase (Spot 2). The bulk LPSO phase was partially dissolved after heat treatment with little overall change. As shown in Fig. 2(a), after the homogenization treatment (Sample IT0), there was only bulk LPSO phase at the grain boundaries, and there was no lamellar LPSO phase in the grains. As shown in Figs. 2(b−d), after the pre-annealing treatment (Samples IT1−IT7), lamellar LPSO phases with different densities appeared in the grains, and the density of these lamellar LPSO phases increased with lengthening annealing time. As shown in Figs. 2(e−h), after the pre-aging treatment, a white second phase appeared at the grain boundaries, which was analyzed via EDS and identified as the Mg5RE phase (Spot 1). The density of the lamellar LPSO phase in the grains slightly increased, and a precipitation-free zone (PFZ) appeared at the grain boundaries because the Mg5RE phase precipitated. The width of the PFZ increased with lengthening annealing time.

After the pre-aging treatment, the β' phase in the grains could not be observed via SEM due to its small size. To observe the difference in the second phase before and after aging, further TEM images were taken. Samples IS0 and IS1 were selected for specific analysis, as shown in Fig. 3. The second phase was analyzed via EDS. The specific composition of 84.58Mg−12.03Gd−1.47Y−0.75Zn−

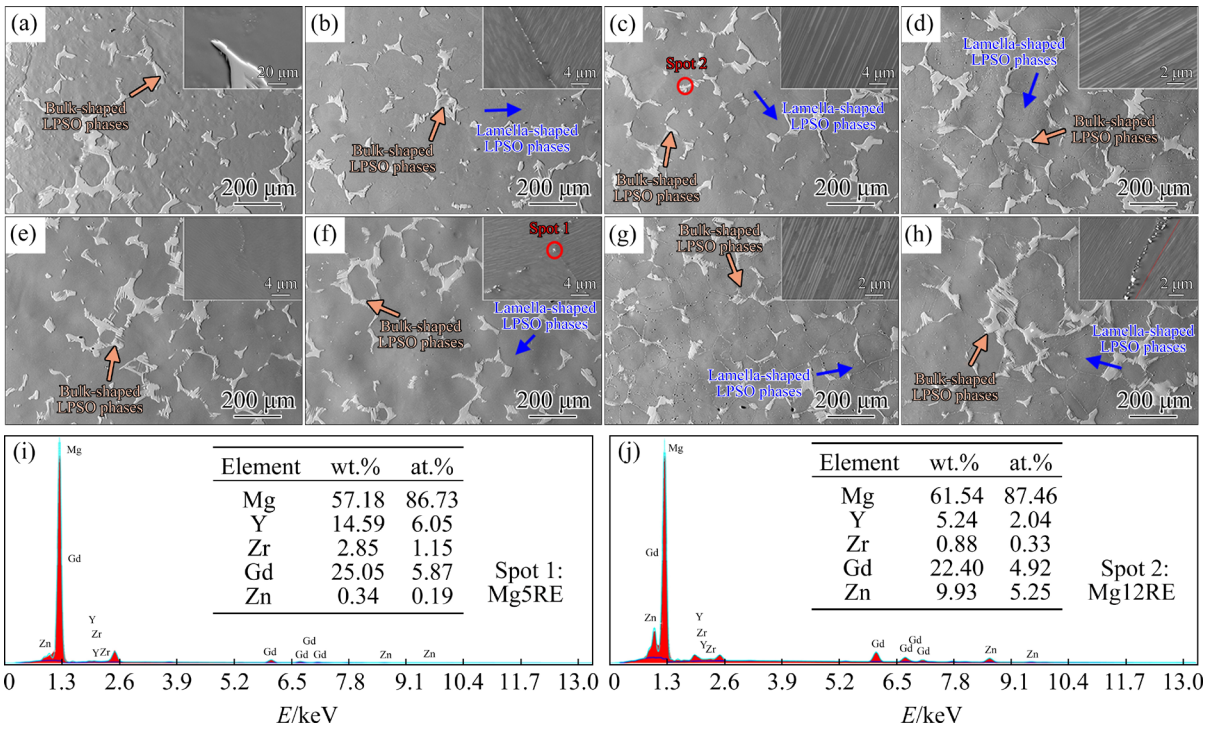

Fig. 2 SEM images of initial samples (a−h), and EDS analysis (i, j): (a) IT0; (b) IT1; (c) IT4; (d) IT7; (e) IS0; (f) IS1; (g) IS4; (h) IS7; (i) Spot 1; (j) Spot 2

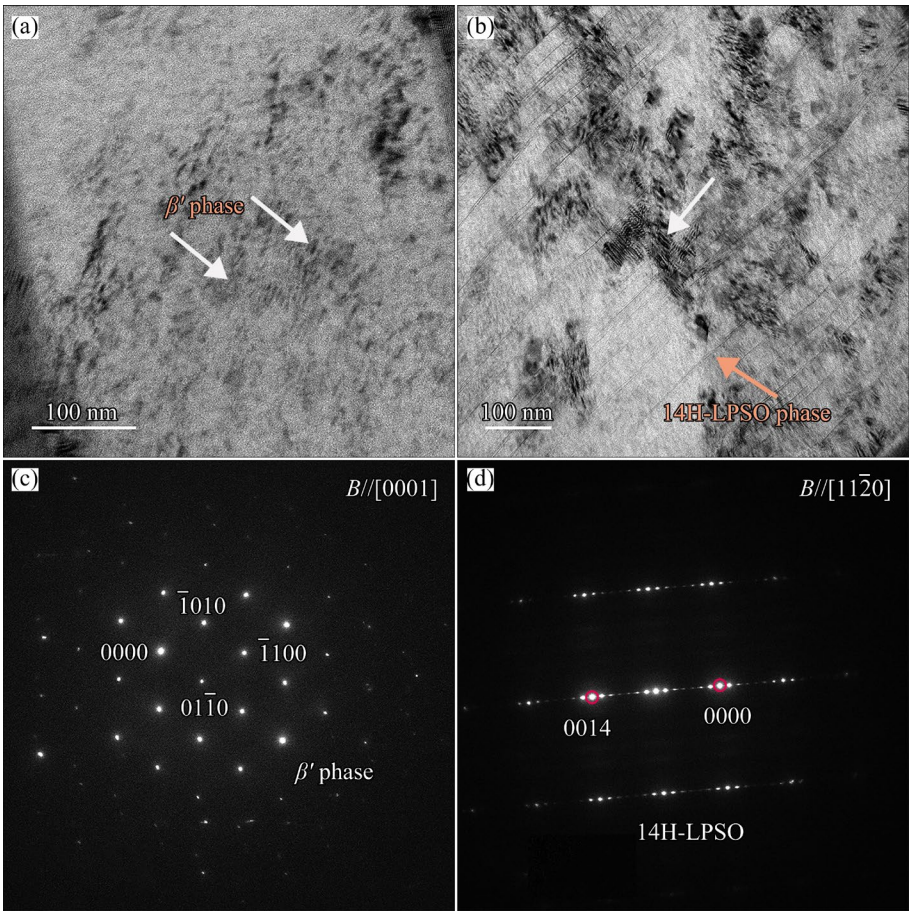

Fig. 3 TEM images (a, b) and corresponding SAED patterns (c, d) of samples: (a) IS0; (b) IS1; (c) β' phase; (d) 14H-LPSO phase

1.17Zr (wt.%) confirms that aging generated the β' phase [11]. For Sample IS0, many β' phases appeared in the grains, but no obvious lamellar LPSO phases were observed. This finding is attributed mainly to the low aging temperature, which failed to provide a sufficient driving force to form the LPSO phase. In contrast, for the IS1 sample, an interlayer structure that consisted of lamellar LPSO and β' phases was observed within the grains. Previous studies [3,11] have shown that the LPSO phase on the basal plane can impede the motion of non-basal dislocations during deformation. The β' phase of prismatic surfaces hinders the motion of basal dislocations [18,19]. We focus on the effects of the reticulation structure formed by these two materials on the microstructure and DRX behavior after thermal compression deformation.

Figure 4 shows the distribution of the LPSO and β' phases after pre-annealing treatment. The density and width of the lamellar LPSO phase inside the grains increased with lengthening pre-annealing time. After the aging treatment, the β' phase precipitated inside the grains and formed a reticulated structure with the LPSO phase. The best effect was observed in Sample IS1. In IS4 and IS7 samples, the expansion of the lamellar LPSO phase in the grains consumed more solid-solution elements, which weakened the aging effect and decreased the size of the β' phase.

3.2 Microstructure after thermal compression deformation

Figure 5 shows the EBSD maps of different samples with the corresponding DRX volume fractions (X_{DRX}). Different colors represent different grain orientations, where black indicates regions unidentified by the software (LPSO phase regions). The black lines denote large-angle grain boundaries (>15°), whereas the white lines represent small-angle grain boundaries (2°−15°). After the thermal

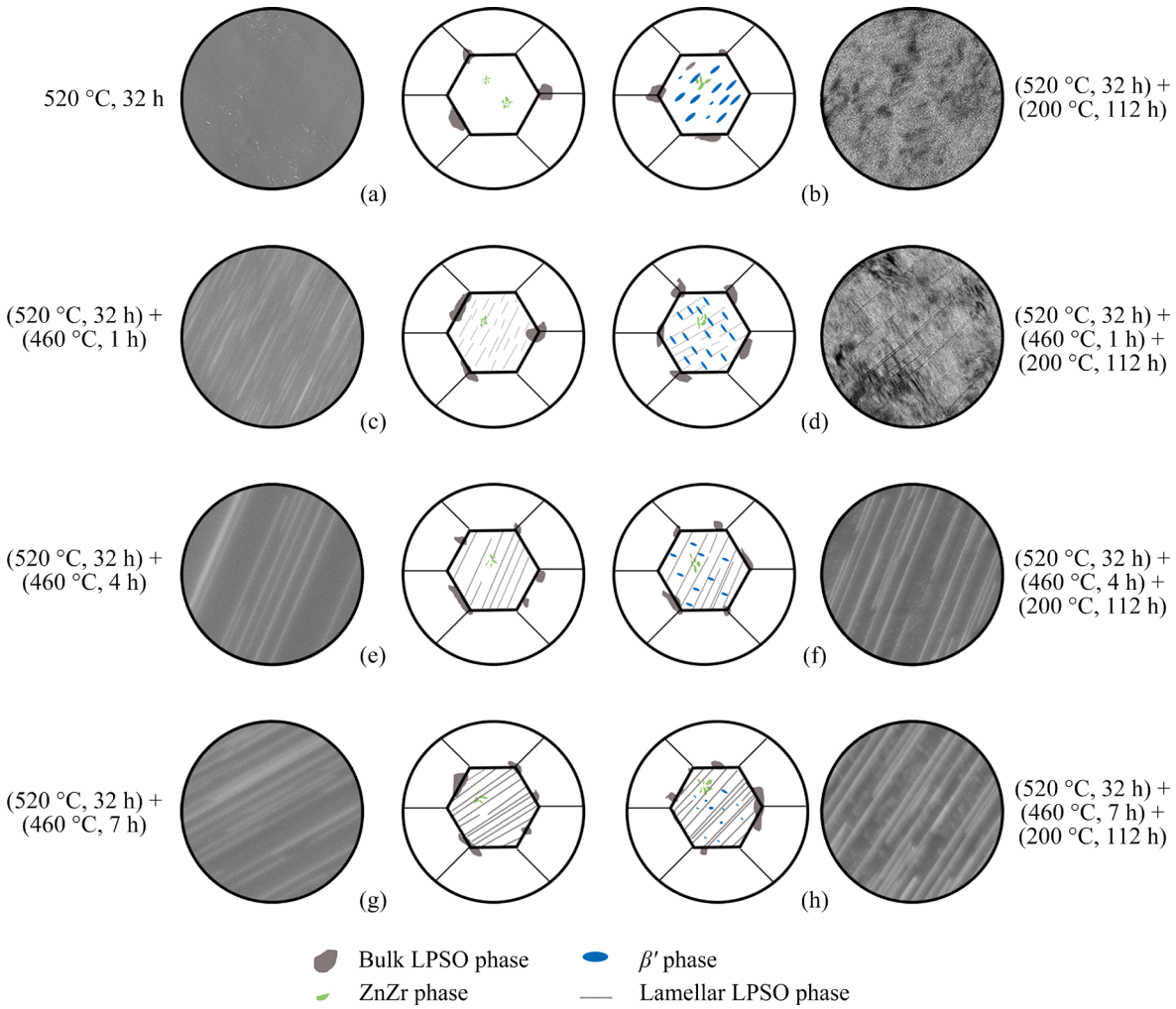

Fig. 4 Schematic distribution of second phase after pre-heating treatment

compression deformation, the coarse grains extended perpendicularly to the compression direction, and the grains became elongated from their original equiaxed shape.

In the annealed samples, the volume fraction of DRX increased after the hot compression, and the average grain size decreased with prolonged annealing time. In contrast, for the aged samples, the volume fraction of DRX did not exhibit a consistent trend with the annealing duration. Instead, it first decreased and subsequently increased. Figures 5(a, e) show significant differences in the overall microstructure with a noticeable increase in the DRX volume fraction and effective grain refinement after aging. Conversely, for the other samples, the DRX volume fraction slightly decreased after the aging treatment, although the overall differences were not significant. Table 2 lists the specific grain sizes.

Figure 6 shows SEM images of different samples. After the thermal compression deformation, the bulk LPSO phase underwent kinking and fragmentation and was distributed perpendicularly to the compression direction. Lamellar LPSO phases appeared inside the grains of all the samples, mostly within the coarse and deformed grains, and kinked to various degrees during the deformation process. LUAN et al [20] investigated the plastic deformation behavior of Mg−4Gd−1Zn−0.5Mn alloys that contained LPSO

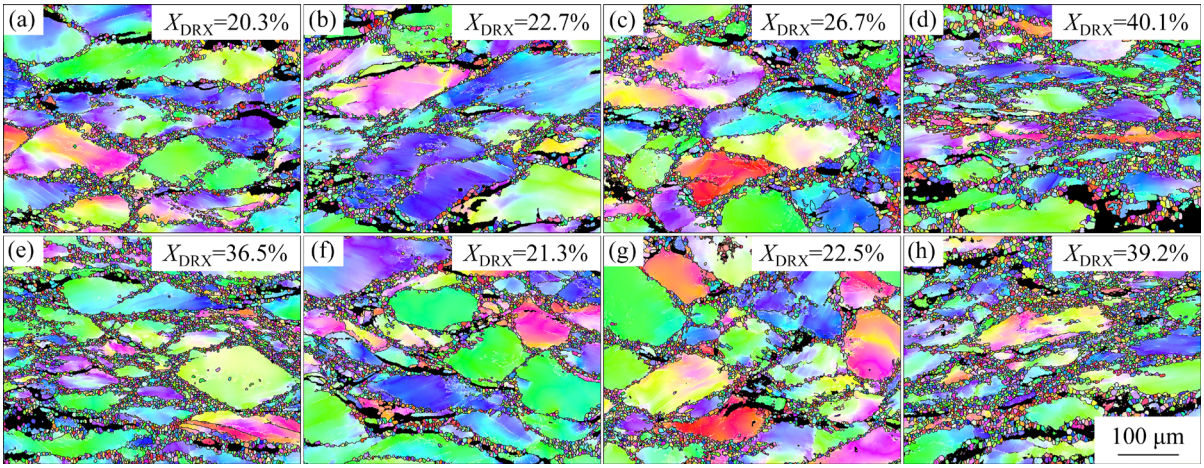

Fig. 5 EBSD maps of samples: (a) T0; (b) T1; (c) T4; (d) T7; (e) S0; (f) S1; (g) S4; (h) S7

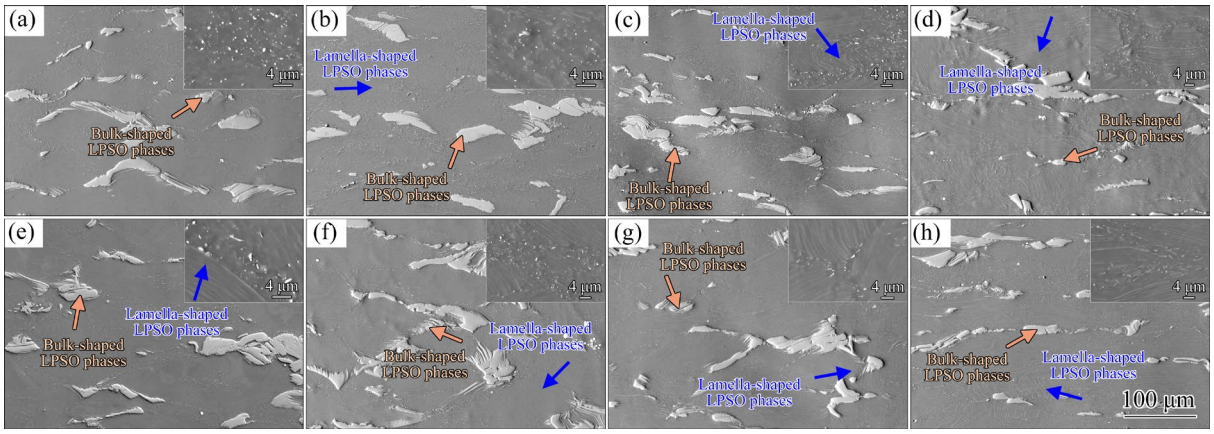

Fig. 6 SEM images of samples: (a) T0; (b) T1; (c) T4; (d) T7; (e) S0; (f) S1; (g) S4; (h) S7

Table 2 Grain sizes of different samples after hot compression (μm)

Grain	T0	T1	T4	T7	S0	S1	S4	S7
Whole grain	70.93	62.05	58.50	31.53	39.29	66.67	63.38	36.17
DRX grain	4.29	4.64	4.96	5.40	4.47	4.37	4.84	5.24

phases under high-temperature compression. They reported that the lamellar LPSO phase hindered grain boundary migration, which delayed DRX, whereas the bulk LPSO phase dissolved, broke up at 500 °C, and acted as heterogeneous nucleation points to effectively promote DRX.

At higher deformation temperatures, the β' phase produced by aging gradually transformed into the β (Mg5RE) phase. The Mg5RE phase was primarily found at the grain boundaries of DRX with dynamic precipitation during deformation. On the one hand, it could effectively pin grain boundaries and inhibit DRX grain boundary migration. On the other hand, when the dynamic precipitation size was large (>1 μm), DRX could be promoted through the PSN mechanism. Under appropriate conditions, dynamic precipitation and DRX can occur in the deformed region. Dynamic precipitation mainly occurs at grain boundaries in the deformed region, and the second-phase particles at the grain boundaries of recrystallized grains can pin these boundaries, which refines the recrystallized grains [21].

3.3 Stress−strain curves

Figure 7 shows the true stress−strain curves of the samples in different states. Figure 7(a) shows the stress−strain curves of the hot compression

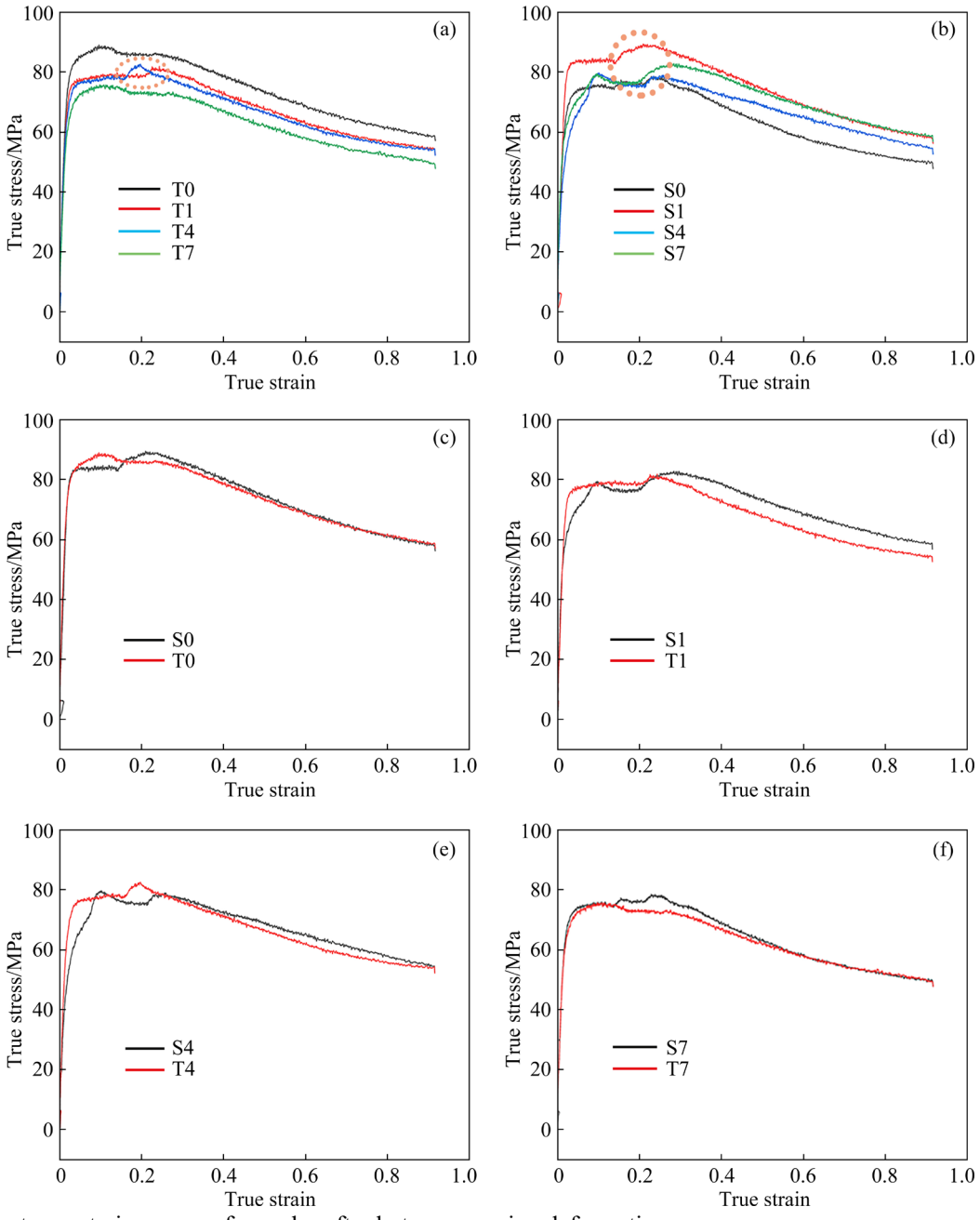

Fig. 7 True stress−strain curves of samples after hot compression deformation

samples after the pre-homogenization and annealing treatment, which can be divided into three main stages: hardening, transition and softening. With increasing strain, the stress first rapidly increases, reaches the peak stress, and subsequently slightly decreases. In the early stage of deformation, the flow stress rapidly and linearly increases with strain because the movement of dislocations rapidly increases the dislocation density. In this stage, the dislocations are insufficient to counteract the work hardening produced by the increased dislocation density, so the flow stress rapidly increases during the hardening stage [22−24]. As the strain increases, dynamic recovery and dynamic recrystallization occur. To accommodate the deformation, the LPSO phase of the alloy undergoes kinking. The softening effect of kinking and the dynamic recrystallization of the LPSO phase partially offset the work-hardening effect, which decreases the work-hardening rate. Owing to the delayed DRX and twinning behavior of the LPSO phase, there is a dynamic competition between softening and work hardening, which leads to a dynamic equilibrium region before the peak stress is reached, and this process corresponds to the transition stage.

As deformation continues, twinning occurs in the alloy and increases the work-hardening capacity until peak stresses are achieved (as indicated by the orange circles). With increasing strain, dynamic recrystallization reoccurs due to the continuous increase in dislocation density and the intensification of lattice distortion. The nucleation and growth of dynamically recrystallized grains consume the dislocations in the material, which makes the softening process dominant. After reaching the peak, the curve decreases at a fast rate, which indicates that DRX is the primary softening mechanism in this stage. Interestingly, when the strain increases, the curve does not exhibit the usual steady-state phase, which suggests that the cumulative strain of this deformation is limited, and the DRX does not completely occur.

Figure 7(b) shows the stress−strain curves of the hot-compression samples after the pre-homogenization, annealing and aging treatment. The curve follows a pattern identical to that in Fig. 7(a), which has three stages: hardening, transition and softening. Figure 7(c) compares the stress−strain curves with and without the pre-aging treatment. The peak stress of the curves after the pre-aging treatment is close to that before the annealing treatment. However, the peak strain slightly shifts back, which indicates that the pre-annealing and aging treatment can suppress DRX during the hot compression process.

4 Discussion

4.1 Driving force model of DRX

DRX is an effective mode of grain refinement in Mg−Gd−Y−Zn−Zr alloys, which weakens the texture and improves the properties. During the deformation process, the local stress concentration is mainly relieved by dynamic recovery (DRV) in the early stage because the accumulated dislocations are initially insufficient to reach the critical conditions to begin DRX. As deformation continues and dislocations accumulate, when the rate of increase in the dislocation density surpasses that at which the dynamic recovery can accommodate, and dynamic recrystallization occurs at the critical point. The corresponding strain and stress at this point are called the critical strain and critical stress, respectively. The DRX model can be expressed via the Avrami equation as follows:

$$X_{\mathrm{DRX}}=1-\exp\left[k\left(\frac{\varepsilon-\varepsilon_{\mathrm{c}}}{\varepsilon^{*}}\right)^{n}\right] \tag{1}$$

where X_{DRX} is the volume fraction of DRX, k and n are constants, ε is the strain, ε_{c} is the critical strain, and ε^{*} is the strain that corresponds to the maximum softening rate of DRX.

The critical point at which dynamic recrystallization (DRX) of the alloy occurs cannot be directly and accurately identified from the stress−strain curve. The onset of DRX was related to the inflection point of the strain hardening rate (θ) versus flow stress (σ) curve [21,25]. If we fit the θ–σ curve from 0 to the peak stress three times, the fitting equation is as follows:

$$\theta=A\sigma^{3}+B\sigma^{2}+C\sigma+D \tag{2}$$

where $\theta=\mathrm{d}\sigma/\mathrm{d}\varepsilon$, and A, B, C and D are constants for a given deformation condition. The θ–σ curves for different states were fitted three times via Origin software, and Fig. 8 shows the results. The critical stress generated by DRX was found at $-\mathrm{d}\theta/\mathrm{d}\sigma=0$ via derivation, which corresponds to the critical stress for DRX, as shown in Table 3.

Table 3 Corresponding critical values under different conditions and volume fractions of DRX

Sample	σ_c/MPa	ε_c	X_{DRX}/%
T0	78.83	0.059	52.21
T1	65.75	0.104	59.19
T4	59.20	0.089	60.70
T7	57.40	0.080	78.3
S0	68.99	0.088	73.33
S1	64.53	0.112	45.80
S4	62.85	0.151	52.14
S7	61.59	0.134	76.52

Since DRX commonly occurs before the peak stress, the work-hardening rate before peak stress was logarithmized, and the ln θ–ε curve was fitted three times. As shown in Fig. 9, the work hardening rate rapidly decreased with increasing strain; when a certain critical value was reached, the curve became smooth with a slight upward trend. This trend is consistent with the phenomenon observed in the stress−strain curve. The inflection point of the ln θ–ε curve represents the critical strain of DRX, which can be determined by taking the first derivative of the curve. The strain at the point where the derivative is zero is the critical strain of DRX. Table 3 shows the specific values.

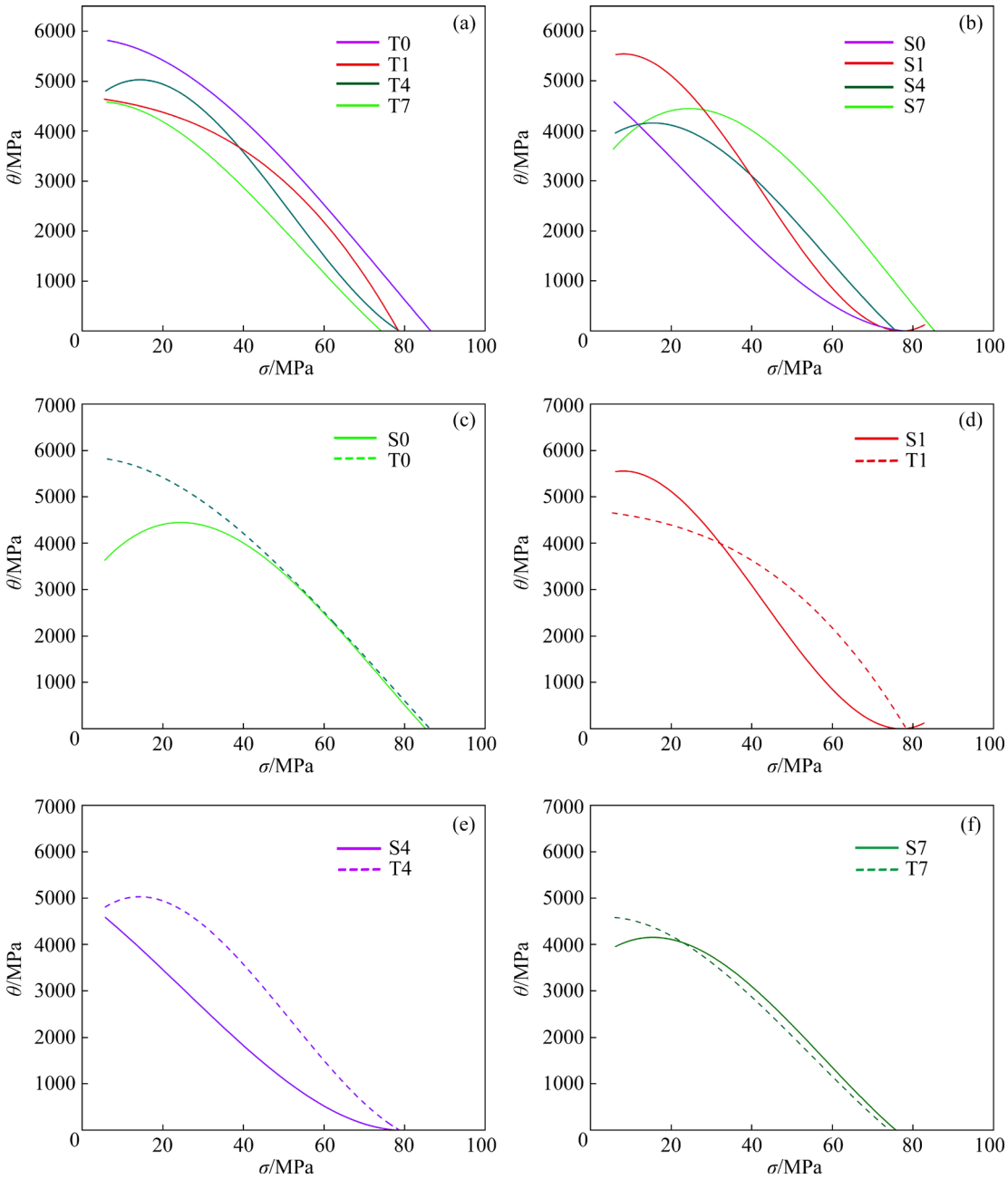

Fig. 8 θ–σ curves of samples

In addition to Eq. (1), Eq. (3) can be used to calculate the volume fraction of DRX:

$$X_{\mathrm{DRX}}=\frac{\sigma_{\mathrm{p}}-\sigma}{\sigma_{\mathrm{p}}-\sigma_{\mathrm{ss}}} \tag{3}$$

where σ_{p} is the peak stress, σ is the stress, and σ_{ss} is the stress when the flow stress curve reaches the stabilization stage. By associating Eqs. (1) and (3), we obtain Eq. (4) and the specific values of the constants k and n.

$$\frac{\sigma_{\mathrm{p}}-\sigma}{\sigma_{\mathrm{p}}-\sigma_{\mathrm{ss}}}=1-\exp\left[k\left(\frac{\varepsilon-\varepsilon_{\mathrm{c}}}{\varepsilon^{*}}\right)^{n}\right] \tag{4}$$

Figure 10 shows the DRX model obtained according to Eq. (1). When the strain increases, the volume fraction of DRX also increases. The volume fraction of DRX gradually increases with lengthening annealing time. The lowest DRX rate in the pre-deformation stage of the T7 sample can be attributed to the lamellar LPSO phase, which effectively strengthens the matrix, dampens the dislocation movement and delays DRX in the early stage. In the later stage of deformation, the LPSO phase coordinates deformation by kinking and breaking. The inhibitory effect of the broken LPSO phase decreases and promotes DRX through the PSN effect.

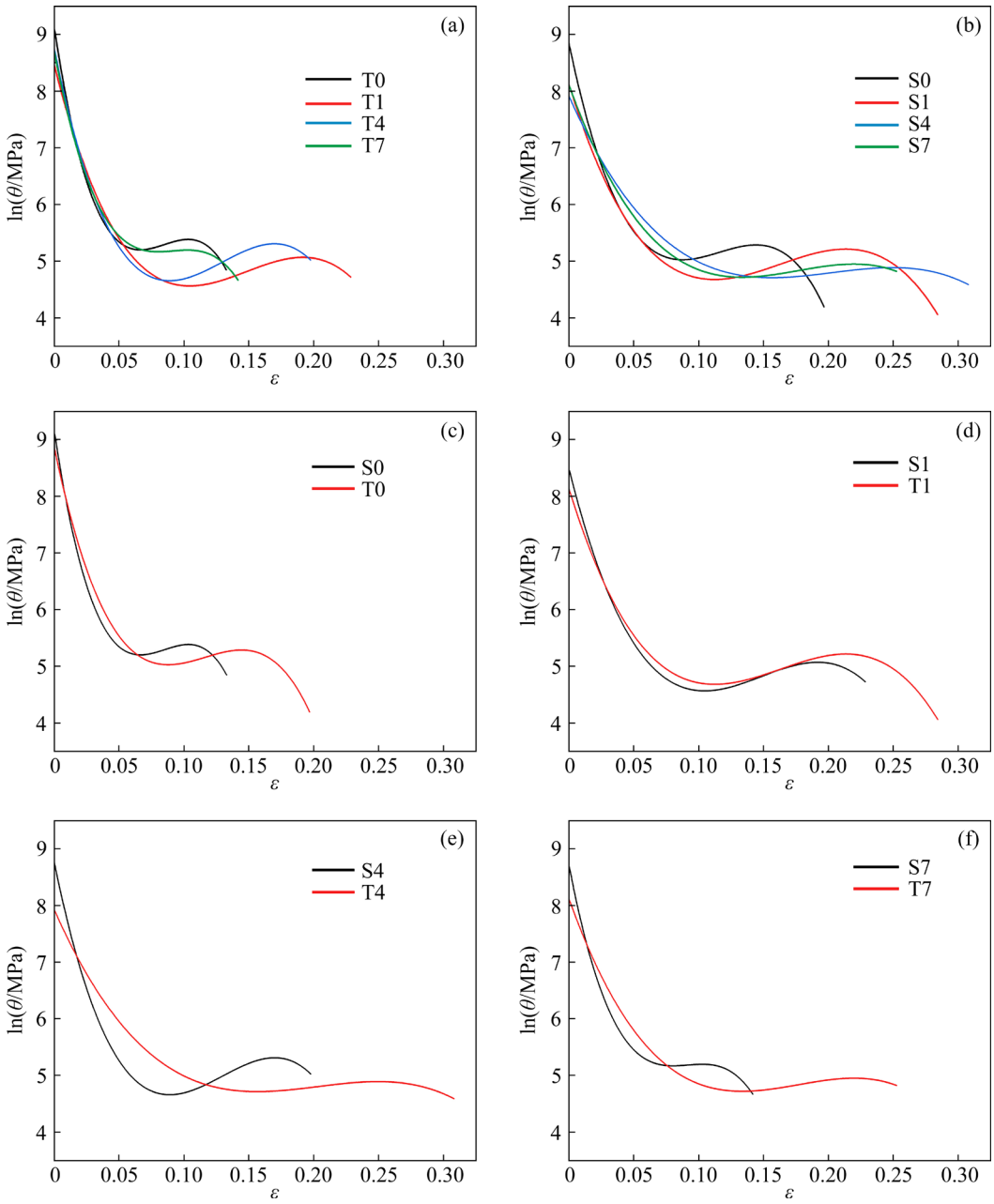

Fig. 9 ln θ–ε curves of samples

As shown in Fig. 10(c), the critical strain for DRX of the sample after the aging treatment increases, and the DRX rate is low in the early stage of deformation. This delay in DRX at the early stage occurs because the β' phase generated after aging hinders the dislocation motion. A comparison of Samples T0 and S0 revealed that the volume fraction of DRX increased after the aging treatment, since the Mg5RE phase effectively promoted DRX through the PSN mechanism, which is consistent with our previous findings [15]. However, for Samples T1−T7, the aging treatment significantly inhibited the occurrence of DRX, which gradually weakened with increasing annealing time. This phenomenon may be related to the interaction between the LPSO phase and the β' phase.

The theoretical volume fraction of DRX is high, which may be due to the neglect of the solute drag effect and pinning effect of the dynamic precipitation. However, the variation rule of the calculated volume fraction of DRX remains consistent with the experimentally observed trend in Fig. 5. The DRX driving force model can better predict the optimal process parameters and provide guidance for experiments.

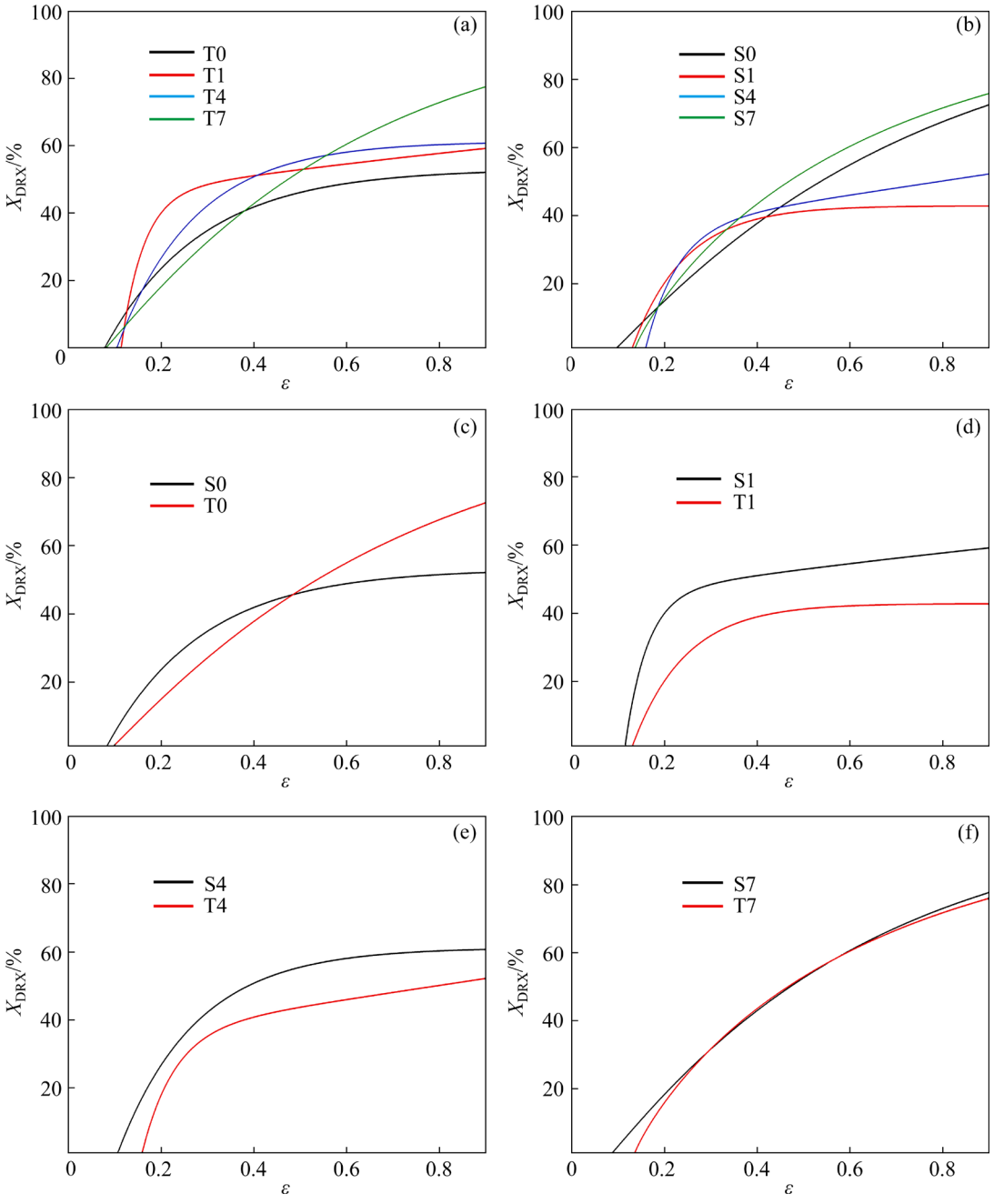

Fig. 10 X_{DRX}−ε curves of samples

4.2 Dynamic recrystallization mechanism

4.2.1 LPSO regulatory mechanism relative to DRX

Figure 5 shows that the volume fraction and average grain size of DRX after hot compression gradually increased with lengthening annealing time (from 20.3% to 40.1% and from 4.29 μm to 5.40 μm, respectively). Studies have demonstrated that the presence of the lamellar LPSO phase retards DRX nucleation and growth. LI et al [26] manipulated the intragranular spacing of the LPSO phase by adjusting the cooling rate after the solid solution heat treatment. The closely spaced LPSO phases suppressed DRX, whereas large spacings promoted non-basal slip and continuous dynamic recrystallization (CDRX). The density of the internal lamellar LPSO phase increased with lengthening annealing time. However, the volume fraction of DRX that corresponded to thermal compression reached its peak.

Typical grains in Samples T0 and T7 were selected for specific analysis of the DRX mechanism. As shown in Fig. 11(a), the internal orientation of the coarse grains in Sample T0 more noticeably changed, which indicates a greater degree of dislocation movement inside the grains, as confirmed in Fig. 11(b). The misorientation angle between Points *A* and *B* was 20°, which clearly validates the CDRX. CDRX is the formation of new DRX grains through the accumulation of dislocations when the dislocations continuously move throughout the deformation process and small-angle grain boundaries gradually transform into large-angle grain boundaries [27−29]. For Sample T7, as shown in Figs. 11(d−f), the internal dislocation density of the grains is low, and there is not much change in the grain orientation across different regions. The maximum orientation difference angle between Points *C* and *D* is only 8°, which indicates that CDRX is not the primary grain refinement mechanism.

Discontinuous dynamic recrystallization (DDRX) involves the formation of subgrain boundaries through dislocation motion, stripping of the locally bowed portion of the grain boundary from the matrix, and growth through the migration of high-angle grain boundaries. As shown in Figs. 11(b, e), the grain boundaries of Sample T7 more obviously bowed outward, and the overall shape was serrated, whereas Sample T0 had smoother grain boundaries. The purple arrows show the locations where DDRX occurred, and DDRX was more likely to occur at Sample T7 than at Sample T0. With increasing annealing time, the

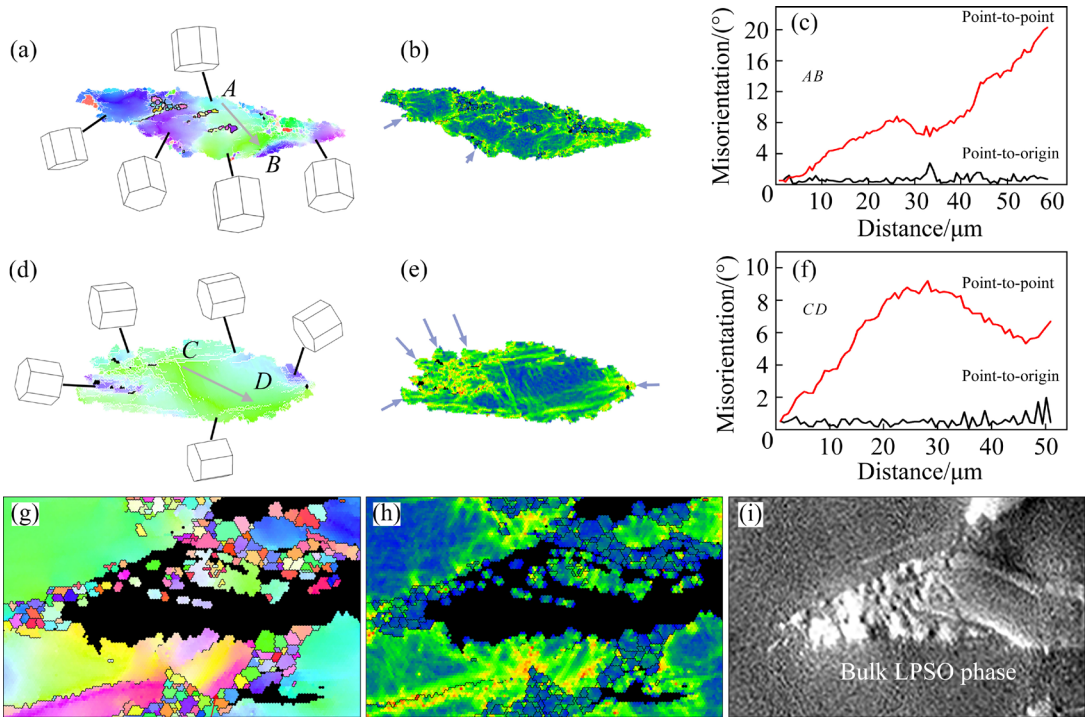

Fig. 11 EBSD results from Fig. 5: (a−c) Sample T0; (d−f) Sample T7; (g−i) PSN mechanism by bulk LPSO phase; (a, d, g) IPF maps; (b, e, h) KAM graphs; (c) Line profiles of misorientation angle along gray arrow *AB* in (a); (f) Line profiles of misorientation angle along gray arrow *CD* in (d); (i) SEM image

lamellar LPSO phase consumes the bulk LPSO phase at the grain boundaries, which leads to its dissolution and fragmentation and promotes grain refinement through the PSN mechanism. As shown in Figs. 11(g−i), the dislocation density around the bulk LPSO phase is high, and many DRX grains are distributed nearby.

4.2.2 Synergistic regulatory mechanism of DRX by LPSO phase and β' phase

A comparison of the DRX volume fraction and average grain size before and after aging revealed interesting trends. For Samples S1−S7, the aging treatment slightly decreased the DRX volume fraction and average grain size. This phenomenon may be attributed to the reticular structure formed by the overlap of the LPSO phase and β' phase, which impedes the movement of dislocations and suppresses the DRX. However, for Sample S0, the volume fraction of DRX significantly increased after the aging treatment (from 20.3% to 36.5%). Additionally, the average DRX grain size slightly increased. In order to elucidate these findings, we conducted further analysis on Samples S0 and S1.

Owing to the large phase spacing of the lamellar LPSO in Sample S0, the hindering effect on dislocation motion was weak. In Figs. 12(a, c) for Sample S0, the misorientation angle along *AB* was 18°, which indicates significant dislocation motion inside the grain, which is a prerequisite for CDRX to occur. In Figs. 12(d, f) for Sample S1, the misorientation angle along *CD* was only 9°, which indicates that the mesh structure composed of the LPSO phase and β' phase can effectively inhibit dislocation motion and suppress the occurrence of CDRX. The corresponding KAM graphs are shown in Figs. 12(b, e), and the KAM values are positively correlated with the dislocation density. Sample S1 had a small dislocation density inside the grains due to the inhibition of dislocation motion by the second phase. Sample S0 had a great dislocation density inside the grains, which confirms the inhibition of the CDRX. DDRX was mainly distributed in the bowing-out area of the grain boundaries, which formed subgrain boundaries through dislocation movement and separated them from the matrix. The two necessary conditions are grain boundary bowing and dislocation movement. The accumulation of dislocations at the grain boundaries of Sample S0 was low, which was unfavorable for DRX.

As depicted in Figs. 13(a, c), the presence of larger Mg5RE phases (>1 μm) at the grain boundaries of Sample S0 promoted DRX through the PSN mechanism. Additionally, as shown in Fig. 13(b), the small size of the Mg5RE phase was insufficient to promote DRX through the PSN mechanism. Instead, it was mostly distributed at the grain boundaries, which inhibited DRX growth by pinning the grain boundaries. There was a slight decrease in the DRX volume fraction (from 22.7% to 21.3%) and a slight increase in the average grain size (from 4.64 to 4.37 μm) after the aging treatment. Owing to the low aging temperature, which prevents the LPSO phase formation, many

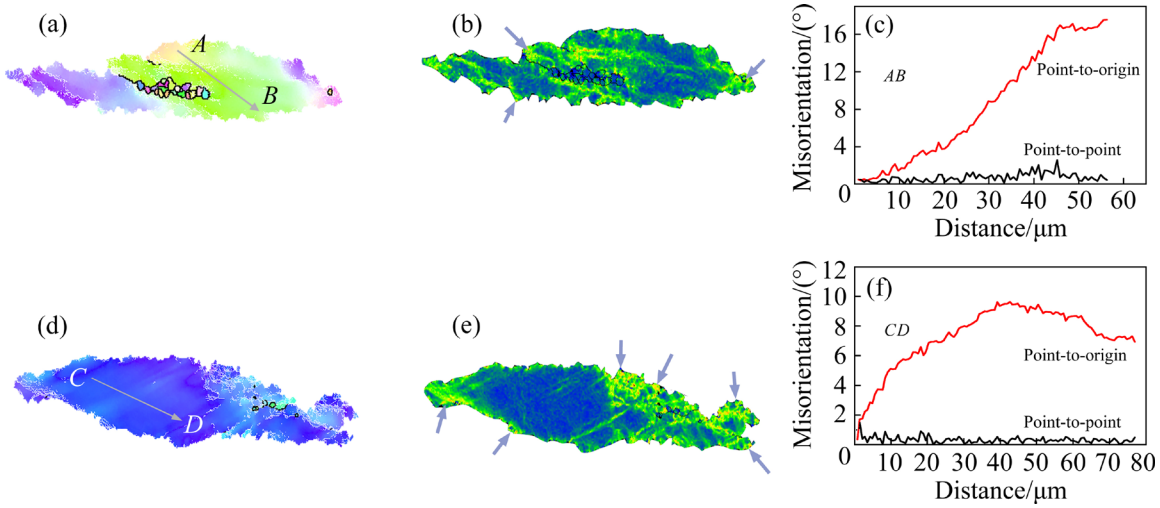

Fig. 12 EBSD results from Fig. 5: (a−c) Sample S0; (d−f) Sample S1; (a, d) IPF maps; (b, e) KAM images; (c) Line profiles of misorientation angle along gray arrow *AB* in (a); (f) Line profiles of misorientation angle along gray arrow *CD* in (d)

Mg5RE phases are generated inside the grains. These phases promote DRX nucleation through the PSN mechanism and can effectively pin the grain boundaries and inhibit grain growth because the phases are smaller than the grains. Figure 13(d) shows that the reticular structure composed of the LPSO phase and β' phase in Sample S1 impedes dislocation movement and causes dislocation accumulation, which is consistent with the results in the KAM graph.

In summary, the grains of Sample T0 were refined primarily through CDRX and effectively pinned by fine dynamic precipitates at the grain boundaries. With increasing annealing time, the bulk LPSO phase dissolved, broke and refined the grains mainly through PSN and DDRX at the grain boundaries. Compared with Sample T0, Sample S0 exhibited a significant increase in the DRX volume fraction, which was attributed primarily to the PSN mechanism (due to the presence of larger-sized Mg5RE phases) and CDRX. The interlayered structure of the LPSO and β' phases in Sample S1 effectively hindered dislocation motion and inhibited the occurrence of CDRX, which enabled DDRX to dominate.

4.3 Synergistic reinforcement of LPSO phase with β' phase

In peak-aged Mg−RE alloys, the β' phase serves as the main precipitated strengthening phase and hinders the dislocation motion during deformation [30]. Compared with those in extruded state alloys, the abundance of nano β' precipitated phases in the aged state alloys enhances their strength and damping properties. After aging, the alloys exhibit significantly increased yield and tensile strengths and improved damping properties [18]. The synergistic interaction between the LPSO phase and nano-β' precipitation phase contributes to the high strength (tensile strength of 374 MPa, and yield strength of 270 MPa) and high plasticity (10.1%) of the Mg−9Gd−1.5Y−0.8Zn−0.3Zr (wt.%) alloy [31]. However, studies on the combined action of these two phases are limited, and further exploration is needed to ascertain whether their synergistic effect can exceed the sum of their individual contributions.

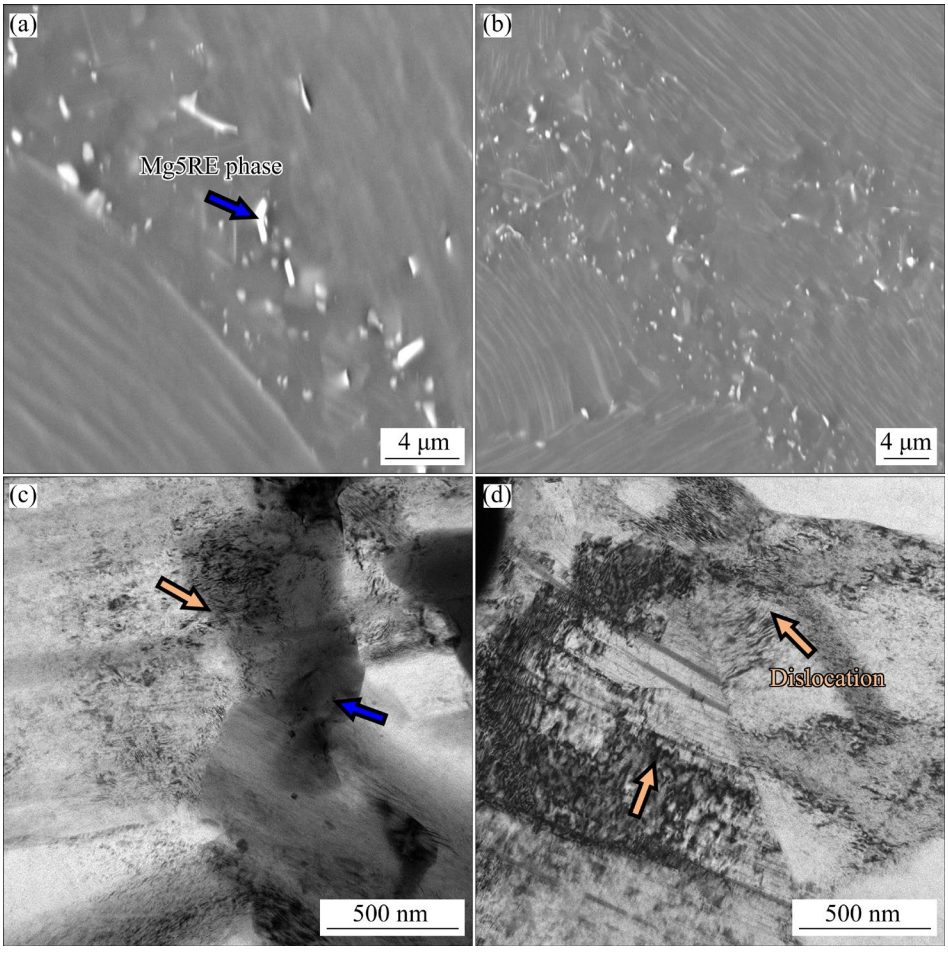

Fig. 13 SEM (a, b) and TEM (c, d) images of Sample S0 (a, c) and Sample S1 (b, d)

For Sample T7, the LPSO phase had the largest width and strongest hindering effect on dislocations. The dislocation density in the grains was relatively high, and the ability to refine the grains was the strongest. The dislocation density of the annealed samples slightly increased after the aging treatment. Sample S1 had few dislocations in the coarse grains, and an interlayered structure, which consisted of the LPSO and β' phases and effectively pinned the dislocations to distribute most of them at the grain boundaries. For Samples T4 and T7, more dislocations existed in the grains. When the annealing time increased, the LPSO phase coarsened and consumed the RE elements dissolved in the matrix, which reduced the β' phase and weakened its pinning effect.

5 Conclusions

(1) After the annealing treatment, the average grain size decreased from 70.93 to 31.53 μm, and the DRX volume fraction increased from 20.3% to 40.1%. After the aging treatment, the average grain size of the Sample S0 decreased to 39.29 μm, and the DRX volume fraction increased by 79.8%. For Samples S1−S7, the average grain size slightly increased, and the DRX volume fraction slightly decreased.

(2) After the aging treatment (Samples S1−S7), the critical equivalent strain of the samples increased. The reticular structure composed of LPSO and β' phases effectively pinned the dislocations and delayed DRX nucleation and growth.

(3) With increasing annealing time (pre-annealing samples), the DRX mechanism changes from CDRX to DDRX+PSN. For Sample S0, owing to the lack of the LPSO phase, the CDRX+ PSN mechanism dominates. For Samples S1−S7, the presence of the reticulation structure inhibited the CDRX, and DDRX dominated.

CRediT authorship contribution statement

Liang LIU: Conceptualization, Data curation, Formal analysis, Writing − Original draft; **Zhi-min ZHANG:** Conceptualization, Methodology, Resources, Writing − Review & editing, Funding acquisition; **Yong XUE:** Conceptualization, Methodology, Writing − Review & editing.

Declaration of competing interest

The authors declare that they have no known competing financial interests or personal relationships that could have appeared to influence the work reported in this paper.

Acknowledgments

This work was supported by the Graduate Education Innovation Program of Shanxi Province, China (No. 2024KY575), and the National Natural Science Foundation of China (No. 52075501).

References

[1] ZHOU Xiao-jie, XIAO Song-ke, LI Miao, WANG Yan-an, LU Xian-zheng, CHEN Zi-jian, GUO Zi-hang, XIAO Hong-chao, GUO Jing. Effect of rotational-die ECAP parameters on microstructure and mechanical properties of Mg97Y2Zn alloys [J]. Journal of Materials Research and Technology, 2024, 29: 3832−3841.

[2] LIU Chao, JI Jin-sheng, ZHENG Jie, WANG Qiang, ZHANG Zhi-min, XUE Yong. Microstructure evolution and mechanical properties of cup-shaped specimens prepared by rotary backward extrusion [J]. Journal of Materials Research and Technology, 2023, 23: 391−402.

[3] CHEN Yi-wen, WANG Jing-ya, ZHENG Wei-sen, LI Quan, YU Ming-di, YING Tao, ZENG Xiao-qin. CALPHAD-guided design of Mg−Y−Al alloy with improved strength and ductility via regulating the LPSO phase [J]. Acta Materialia, 2024, 263(0): 119521.

[4] YAN Zhao-ming, LI Lu-yao, ZHU Jia-xuan, REN Lu-ying, XUE Yong, WANG Qiang, ZHANG Zhi-min. Deformation behavior of LPSO phases, grain refinement mechanism, and texture evolution of a Mg−Gd−Y−Zn−Zr alloy processed by forward extrusion combined with dual-directional angular deformation [J]. Journal of Materials Research and Technology, 2024, 28: 4131−4141.

[5] LIU Yun-fang, LU Dong-liang, WU Guo-qin, ZHANG Zhi-min, HUANG Hua-gui, LI Lin-lin, FENG Yan, YU Jian-min. Deformation mechanism and hardening behavior of gradient heterostructured magnesium alloys prepared by severe shear deformation [J]. Journal of Alloys and Compounds, 2024, 985: 174099.

[6] ZHENG Ce, CHEN Shuai-feng, CHENG Ming, ZHANG Shi-hong, LI Ying-ju, YANG Yuan-sheng. Long-period stacking ordered phase kinking, twinning behavior and dynamic recrystallization of Mg−Gd−Y−Zn−Zr alloy under severe shear deformation [J]. Journal of Alloys and Compounds, 2024, 976: 173239.

[7] XIA Xiang-sheng, SHU Da-yu, YANG Ec-huan, HU Chuan-kai. A comparative study of the role of Zn in microstructures and the mechanical properties of Mg−Gd−Y−Zr alloys [J]. Journal of Materials Research and Technology, 2023, 25: 2903−2912.

[8] LIU Wei, ZHAO Yu-hong, ZHANG Yun-tao, SHUAI Chuan, CHEN Li-wen, HUANG Zhi-quan, HOU Hua. Deformation-

induced dynamic precipitation of 14H-LPSO structure and its effect on dynamic recrystallization in hot-extruded Mg−Y−Zn alloys [J]. International Journal of Plasticity, 2023, 164(0): 103573.

[9] ZHANG Na-na, LIU Ming-ming, LI Qua-nan, CHEN Xiao-ya, ZHENG Ze-yu. Effect of long-period stacking ordered phase on dynamic recrystallization in Mg−Y−Zn−Zr alloy processed by backward extrusion [J]. Journal of Materials Research and Technology, 2023, 26: 2384−2393.

[10] ZHOU Jian-xin, YANG Hong, XIAO Jian-fei, JIANG Bin, LUO Xiao-jun, XIE Wen-long, LI Wei, DONG Zhi-hua, SONG Jiang-feng, XU Jun-yao, HUANG Guang-sheng, ZHANG Ding-fei, PAN Fu-sheng. Optimizing LPSO phase to achieve superior heat resistance of Mg−Gd−Y−Zn−Zr alloys by regulating the Gd/Y ratios [J]. Journal of Materials Research and Technology, 2023, 25: 4658−4673.

[11] LI Lian-hui, YANG Yi-qiang, YAO Hang-tian, LIU Wen-hong, SHA Jian-chun, QIAO Ming-liang, TIAN Jie, BAO Jia-xin, ZHANG Zhi-qiang. Effect of Sn microalloying on microstructure and mechanical properties of Mg−11Gd−1Zn−0.5Zr alloy [J]. Materials Science and Engineering: A, 2024, 891(0): 146018.

[12] WANG Xu, LI Ming, HUANG Yuan-chun, LIU Yu, HUANG Chang-qing. Deformation behavior of LPSO phases with regulated morphology and distribution and their role on dynamic recrystallization in hot-rolled Mg−Gd−Y−Zn−Zr alloy [J]. Journal of Materials Research and Technology, 2023, 26: 6121−6134.

[13] JI Z K, QIAO X G, YUAN L, CONG F G, WANG G J, ZHENG M Y. Exceptional fracture toughness in a high-strength Mg alloy with the synergetic effects of bimodal structure, LPSO, and nanoprecipitates [J]. Scripta Materialia, 2023, 236(0): 115675.

[14] MENG Mu, ZHANG Hong-lei, GAO Zhi, LEI Gen-xing, YU Jian-min. Effect of aging treatment on the precipitation transformation and age hardening of Mg−Gd−Y−Zn−Zr alloy [J]. Journal of Magnesium and Alloys, 2023, 11(12): 4628−4643.

[15] ZHENG Jie, CHEN Zhe, YAN Zhao-ming, ZHANG Zhi-min, WANG Qiang, XUE Yong. Preparation of ultra-high strength Mg−Gd−Y−Zn−Zr alloy by pre-ageing treatment prior to extrusion [J]. Journal of Alloys and Compounds, 2022, 894(0): 162490.

[16] KANG Wei, LU Li-wei, FENG Long-biao, LU Feng-chi, GAN Chun-lei, LI Xiao-hui. Effects of pre-aging on microstructure evolution and deformation mechanisms of hot extruded Mg−6Zn−1Gd−1Er Mg alloys [J]. Journal of Magnesium and Alloys, 2023, 11(1): 317−328.

[17] DANG Cong, DOU Xiao-xu, WANG Jing-feng, YU Di, WANG Jin-xing, LU Ruo-peng, HOU Hua, ZHAO Yu-hong. Investigations on microstructure and mechanical properties of cast Mg−Gd−Y−Zn−Zr−Nd alloy [J]. Journal of Materials Research and Technology, 2023, 24: 4852−4862.

[18] DANG Cong, WANG Jing-feng, WANG Jin-xing, YU Di, ZHENG Wen-xuan, WANG Zi-hong, FENG Le, XU Chang-bing, HOU Hua, ZHAO Yu-hong. The effect of β' precipitates on mechanical properties and damping capacity in the Mg−Gd alloy [J]. Vacuum, 2023, 215(0): 112230.

[19] ZHANG Chao-sheng, ZHAO Si-cong, LI Jing-fang, FENG Yi-cheng, WANG Lei, WANG Zhi-wei, GUO Er-jun. Precipitation behavior and mechanical properties of Mg−Nd−Sm−Zn−Zr alloy [J]. Journal of Materials Research and Technology, 2024, 28: 3385−3395.

[20] LUAN Shi-yu, ZHANG Lei, CHEN Li-jia, MA De-qing, WANG Jin-hui, JIN Pei-peng. Plastic contribution via DRX induced by kink and twin in a hot compressed Mg−Gd−Zn−Mn alloy with 14H LPSO [J]. Materials Science and Engineering: A, 2023, 873(0): 145022.

[21] WANG Ling-hao, JALAR Az-man, DAN Long-hong. Dynamic precipitation and dynamic recrystallization behaviors of Mg−Gd−Nd−Zr magnesium alloy during thermal compression deformation [J]. Journal of Materials Research and Technology, 2023, 26: 7634−7648.

[22] PAN Jin-qi, ZHANG Wen-cong, LI Huan, YANG Jian-lei, ZHANG Zan, WANG Song-hui. Microstructure characteristics, yield asymmetry and fracture mechanism of the fine grained thin-wall Mg−6.03Zn−0.55Zr tubes fabricated by hot spinning [J]. Journal of Alloys and Compounds, 2024, 983: 173841.

[23] MALIK A, BHATTI T M, NAQVI S Z H, ABRAR S, NAZEER F, AL-SEHEMI A G. A new way to analyze constitutive analysis and its relation to the microstructure of a Mg−Gd−Y−Zn alloy [J]. Journal of Alloys and Compounds, 2024, 977(0): 173456.

[24] HUANG Ying-jie, WAN Ying-chun, LIU Chu-ming, JIANG Shu-nong, GAO Yong-hao, CHEN Zhi-yong. Effect of forging temperature on the microstructure, subsequent aging precipitation behavior, and mechanical properties of Mg−Gd−Y−Zr−Ag alloy [J]. Journal of Materials Science & Technology, 2024, 181(14): 41−57.

[25] ZHAO Li, HAO Jian-qiang, LIU Cui-rong, GUI Hai-lian, ZHANG Jin-shan, WANG Hong-xia, CHENG Wei-li. Hot compression behavior of Mg−Zn−Y−Mn−Ti magnesium alloy enhanced by lamellar LPSO phase and spherical W phase [J]. Journal of Materials Research and Technology, 2023, 25: 4784−4798.

[26] LI Ji-yu, WANG Fu-lin, ZENG Jian, ZHAO Chao-yu, JIN Li, DONG Jie. Effect of the interspacing of intragranular lamellar LPSO phase on dynamic recrystallization behaviors of Mg−Gd−Y−Zn−Zr alloys [J]. Materials Characterization, 2022, 193(0): 112326.

[27] JIA Jing-jing, ZHANG Hong-lei, MENG Mu, YANG Xue, ZHANG Xu-hui, ZHANG Zhi-min. Strain-induced heterogeneous bimodal microstructure behavior of Mg−Gd−Y−Zn−Zr alloy containing LPSO phase during hot compression [J]. Journal of Materials Research and Technology, 2023, 27: 4264−4277.

[28] FENG Yun-duo, LUAN Shi-yu, LIU Qiang-bing, LIU Ya-fei, WANG Jin-hui. Microstructures evolution and mechanical properties of dilute Mg−Y−Al−Ca−Mn alloy during uniaxial compression deformation at different strain levels [J]. Materials Today Communications, 2024, 38: 108455.

[29] WU Yi-ping, JIA Yu-zhen, ZHANG Sha, LIU Yu, XIONG Han-qing, CHEN Gang. Flow softening and dynamic recrystallization behavior of a Mg−Gd−Y−Nd−Zr alloy under elevated temperature compressions [J]. Journal of Magnesium and Alloys, 2023, 11(8): 2891−2900.

[30] XU Jian, ZHENG Jie, LIU Wan-er, HUANG You-wang,

YAN Zhao-ming, ZHANG Zhi-min, WANG Qiang, XUE Yong. Recrystallization behavior and strengthening mechanism of extruded Mg−Gd−Y−Zn−Zr alloy with different pre-aged states [J].Transactions of Nonferrous Metals Society of China, 2024, 34(2): 480−503.

[31] DENG Dai-yi, CHENG Ren-ju, DONG Zhi-hua, JIANG Bin, YANG Ming-bo, WANG Hai-jun, YU Chun-tang, MA Yan-long, PAN Fu-sheng. High strength and ductility of cast Mg−9Gd−1.5Y−0.8Zn−0.3Zr alloy achieved by micro-structural regulation [J]. Progress in Natural Science: Materials International, 2023, 33(6): 797−803.

不同预热处理对热压缩 Mg−Gd−Y−Zn−Zr 合金动态再结晶行为的影响

刘 靓，张治民，薛 勇

中北大学 材料科学与工程学院，太原 030051

摘 要：选择 Mg−13Gd−4Y−2Zn−0.5Zr(质量分数，%)合金作为实验材料。经过预热处理后，获得不同 LPSO 相和 β'相分布的初始显微组织，随后进行热压缩实验。研究第二相对显微组织以及动态再结晶(DRX)行为的影响。结果表明，预退火处理后，平均晶粒尺寸从 70.93 μm 减小到 31.53 μm，DRX 体积分数从 20.3%增加到 40.1%。S0(预时效)样品的平均晶粒尺寸减小到 39.29 μm，DRX 体积分数增加了 79.8%，而 S1~S7(预退火+时效)样品的平均晶粒尺寸略有增大，DRX 体积分数略有减小。随着预退火时间的延长，片状 LPSO 相的宽度增加，在变形过程中产生的动态析出减少，钉扎作用减弱。DRX 机制从 CDRX(均匀化样品)转变为 PSN+DDRX(预退火样品)。经过预时效处理后，网状结构有效地钉扎了位错，延迟了 DRX 晶粒的成核和生长，DRX 机制从原来的 CDRX+PSN(预时效样品)转变为 DDRX(预退火+时效样品)。

关键词：Mg−Gd−Y−Zn−Zr 合金；动态再结晶；热压缩；β'相；LPSO 相

(Edited by Xiang-qun LI)